Supporting Information

Photoinduced electron transfer-driven emission enhancement in solid-state viologen hybrids

*Ksenia Chaykun,[*1] Benny Febriansyah,[*2] Trang Thuy Nguyen,[3] Teddy Salim,[4] Yulia Lekina,[5] Ying Sim[1], Yongxin Li,[6] Shuzhou Li,[4] Jinghua Teng,[7] Nripan Mathews,[4] and Zexiang Shen*[1,2,5]*

1. Interdisciplinary Graduate Program, Energy Research Institute@NTU, Nanyang Technological University, 50 Nanyang Avenue, Singapore 639798, Singapore
2. Division of Physics and Applied Physics, School of Physical and Mathematical Sciences, Nanyang Technological University, 50 Nanyang Avenue, Singapore 637371, Singapore
3. Faculty of Physics, University of Science, Vietnam National University, Hanoi, 334 Nguyen Trai, Thanh Xuan, Hanoi, 11416, Vietnam
4. School of Materials Science and Engineering, Nanyang Technological University, 50 Nanyang Avenue, Singapore 639798, Singapore
5. The Photonics Institute and Center for Disruptive Photonic Technologies, Nanyang Technological University, 50 Nanyang Avenue, Singapore 639798 Singapore
6. Division of Chemistry and Biological Chemistry, School of Physical and Mathematical Sciences, Nanyang Technological University, 21 Nanyang Link, 637371, Singapore
7. Institute of Materials Research and Engineering, Agency for Science, Technology, and Research (A*STAR), 2 Fusionopolis Way, Singapore 138634, Singapore

Experimental methods

Materials synthesis

Chemicals. Methyl viologen dichloride (98%), benzyl viologen dichloride (97%), iron(II) chloride (anhydroBeads™, −10 mesh, 99.99% trace metals basis), manganese(II) chloride (anhydroBeads™, −10 mesh, 99.99% trace metals basis), zinc chloride (anhydrous, powder, ≥99.995% trace metals basis), cobalt(II) chloride (anhydroBeads™, −10 mesh, 99.995% trace metals basis), nickel(II) chloride (anhydrous, powder, 99.99% trace metals basis), dimethyl sulfoxide (anhydrous, ≥99.9%) were obtained from Sigma-Aldrich, while acetone (anhydrous; max. 0.01% H_2O; ≥99.8%) was bought from VWR Chemicals.

Growth of single crystals [BnzV][MCl_4].

Stoichiometric amounts of benzyl viologen dichloride [BnzV]Cl_2 and the corresponding metal(II) chloride (MCl_2) were dissolved in anhydrous DMSO inside an inert-atmosphere glovebox.

A typical procedure is as follows: [BnzV]Cl_2 (20.5 mg, 0.050 mmol) and MCl_2 (0.050 mmol; $FeCl_2$: 6.3 mg, $MnCl_2$: 6.3 mg, $CoCl_2$: 6.5 mg, $NiCl_2$: 6.5 mg, $ZnCl_2$: 6.8 mg) were dissolved in 0.60 mL of anhydrous DMSO in a 4 mL glass vial until a clear solution was obtained.

The vial was then placed inside a 20 mL glass container containing 10 mL of dry acetone, which served as an antisolvent. The container was sealed to allow slow vapor diffusion of acetone into the precursor solution. Single crystals formed over 24–48 h at room temperature without further agitation.

The crystals were isolated by decanting the mother liquor, washed three times with 0.5 mL of cold acetone, and dried under reduced pressure (≈10^{-2} mbar) for 20–30 min. The resulting crystals were used directly for structural analysis, with typical isolated yields of 60–75% depending on the metal center.

Each sample was then subjected to single crystal X-ray diffractometers for structure determination. To confirm that the organic cation does not undergo any chemical or structural changes during the single crystals synthesis, ^{1}H nuclear magnetic resonance spectroscopy was also performed with the resulting spectra being presented in **Figure S16**.

Instrumentations and methods

X-ray crystallography. Crystals were mounted on a Bruker X8 Quest CPAD area detector diffractometer, and data were collected using a IμS 3.0 Microfocus Mo−Kα radiation source (λ = 0.71073 Å) at cryogenic temperatures (100 K). Data reduction and absorption corrections were performed using the SAINT and SADABS software packages, respectively. All structures were solved by direct methods and refined by full-matrix least-squares procedures on F2 , using the Bruker SHELXTL-2014 software package. Non-hydrogen atoms were anisotropically refined, after which hydrogen atoms were introduced at calculated positions, and the data further refined. The graphical illustrations of crystal structures used throughout the main paper and the Supporting Information were created using the program VESTA.[1]

Raman and steady-state photoluminescence (SSPL) spectroscopies. A WITec Alpha 300RAS confocal Raman microscope was used to record photoluminescence (PL), Raman. The 532 nm (green) line from laser coupled to an Acton spectrometer with a diffraction grating of 1800 grooves mm^{-1} (1.3 cm^{-1} resolution) and a thermo-electrically cooled Andor CCD detector was chosen to avoid photoluminescence. The backscattered Raman signal passed through two 532 nm BragGrate Notch Filters (BNF) for effective laser line rejection. The UV (325 nm) and blue lines of a linearly polarised CW solid laser (442, 457 nm) were chosen for PL measurements as well as 633 and 532 nm lasers. The excitation power was maintained below 0.5 mW to avoid sample degradation; most measurements were done with 40-45 μW excitation; for power-dependent measurements, several points were chosen in the 0-0.5 mW range. All data were measured between 400 K and 78 K using a nitrogen gas flow cryostat. Room temperature data was measured with open-air media.

Nuclear Magnetic Resonance (NMR) spectroscopy. ^{1}H NMR spectra of organic compounds were recorded in DMSO-d6 solution using a Bruker Avance 400 spectrometer. Chemical shift values (ppm) are referenced against residual protic solvent peaks.

Thermogravimetric Analysis. The thermal analyses were performed using a TA Instruments TGA Q2950 and Q500 models. Samples were heated from room temperature to 400 °C in nitrogen (N_2) with a heating rate of 5 °C/min and flow rate of 60 mL/min.

Differential Scanning Calorimetry. Differential Scanning Calorimetry. Differential Scanning Calorimetry (DSC) measurements were performed employing a TA Instruments Q10 DSC apparatus. The samples underwent analysis in alumina pans and were subjected to heating from -80°C to 180°C at a heating rate of 10°C per minute under a nitrogen atmosphere in a glove box.

UV-vis spectroscopy. UV-vis spectra of polycrystalline samples were collected using a Shimadzu UV-3600 UV-VIS-NIR Spectrophotometer with $BaSO_4$ as the 100% reflectance reference. The measurements were conducted in a 300 – 800 nm wavelength range, with a scanning resolution of 0.5 nm s^{-1}, in the diffuse reflectance mode, using an integrating sphere. Relative absorbance was obtained from Kubelka−Munk transformation of the reflectance spectra: $\alpha/S = (1 - R)^2(2R)^{-1}$, where R is the reflectance, and α and S are the absorption and scattering coefficients, respectively.

X-ray photoelectron spectroscopy (XPS). XPS analysis was performed using an AXIS Supra spectrometer (Kratos Analytical Inc., UK) equipped with a hemispherical analyser and a monochromatic Al K-alpha source (1487 eV) operated at 15 mA and 15 kV. The XPS spectra were acquired from an area of 700 x 300 μm^2 with a take-off angle 90°. Pass energy of 160 eV and 20 eV were used for survey and high-resolution scans, respectively. A 3.1-volt bias was applied to the sample to neutralise charge buildup on the sample surface.

Density-functional theory (DFT) calculation of $[BnzV]^{2+}$ and $[BnzV]^{\bullet+}$. Raman spectra of benzyl viologen cation were computed using DFT within the Gaussian software package. Calculations were performed at the B3LYP/6-311++G(d,p) level to accurately describe vibrational modes in the solid phase. Harmonic frequency calculations provided Raman shifts and intensities, with a scaling factor (~0.98) applied to correct systematic deviations. No solvent model was used to reflect the experimental conditions. Normal mode analysis was conducted using GaussView for vibrational assignment, and the computed spectra were compared with experimental data to validate peak assignments.

DFT calculation of $[BnzV][FeCl_4]$ electronic structure. The DFT methods implemented in the Vienna *ab initio* Simulation Package (VASP)[2-4] were utilised to calculate the electronic structure of the $BnVFeCl_4$ compound. The PBE functional[5] represented the electron exchange-correlation with a Coulomb on-site correction to enhance the treatment of the electron correlation, PBE+U method.[6] The Coulomb on-site potential U = 6 eV was added to the Fe 3d

states. The dispersion interactions were taken into account using the DFT-D3 method.[7] The core electrons were handled under the frozen-core approximation, while the valence electrons were represented employing a plane-wave basis set with a 500 eV energy cutoff. The oscillatory component of the wavefunction was described through the projector augmented wave (PAW) method.[2,3] The Monkhorst-Pack grid of $2 \times 2 \times 4$ was employed for k-point sampling. The self-consistent solution of the Kohn-Sham equations was achieved with a convergence criterion for the total energy set at 10^{-6} eV, and the atomic structure was optimised until the atomic forces were below 0.01 eV/Å.

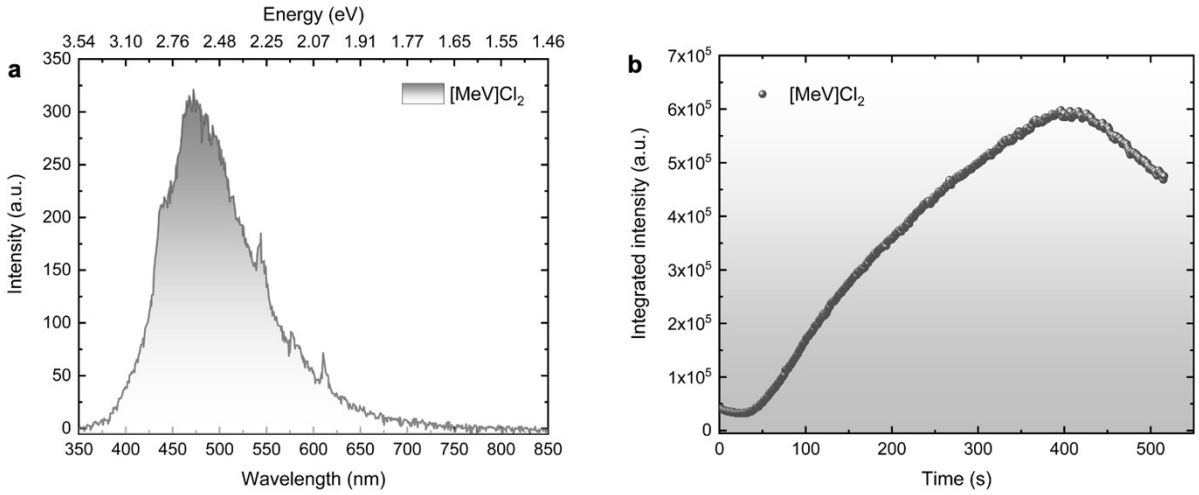

Figure S1. a) Room temperature steady-state photoluminescence (PL) spectrum of methyl viologen dichloride ([MeV]Cl_2) single crystal excited with 325 nm wavelength. b) Time-dependent integrated PL intensity of [MeV]Cl_2 under continuous 325 nm light irradiation.

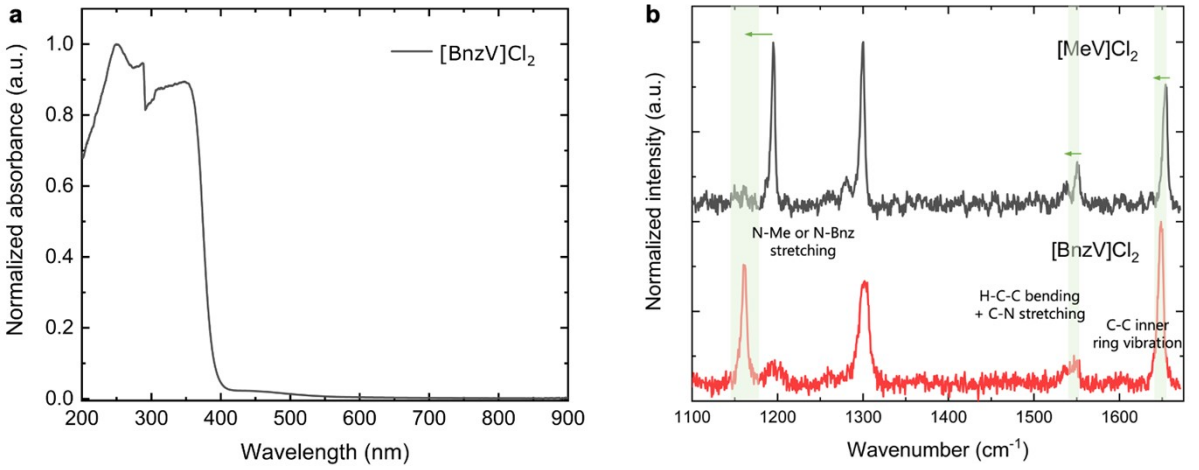

Figure S2. a) Absorption spectra of polycrystalline powder of [BnzV]Cl_2. b) Raman spectra comparison of methyl viologen dichloride ([MeV]Cl_2) and benzyl viologen dichloride ([BnzV]Cl_2). Peaks related to the pyridinium ring get shifted to lower energy, suggesting some intermolecular interaction (*e.g.,* π-π stacking) in [BnzV]Cl_2 lattices.

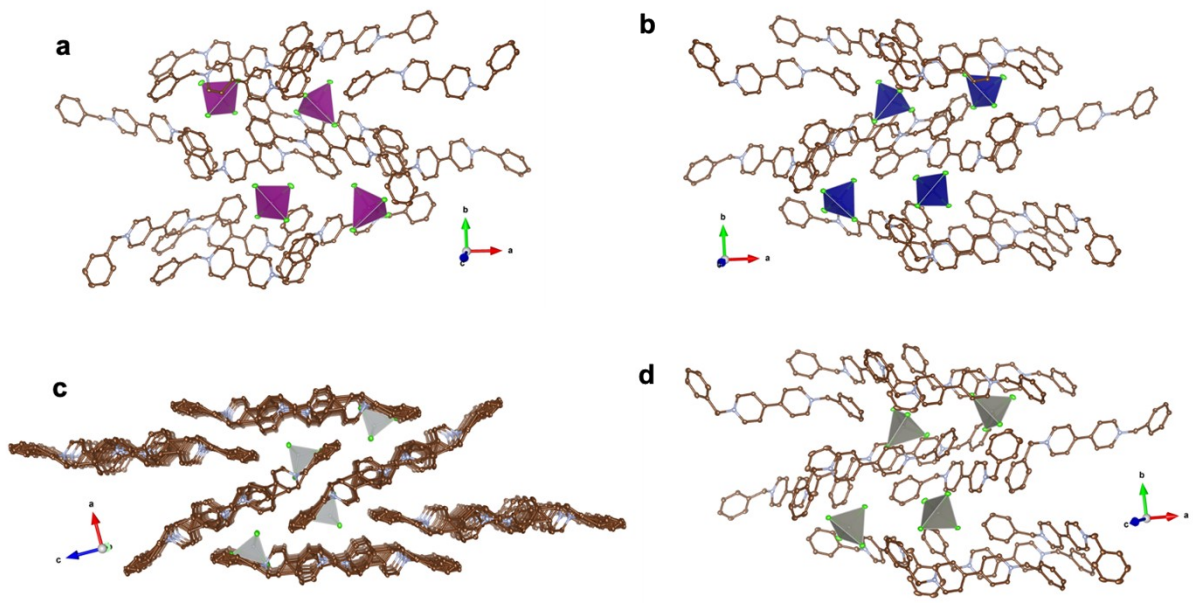

Figure S3. Single crystal X-ray structures of a) [BnzV][$MnCl_4$], b) [BnzV][$CoCl_4$], c) [BnzV][$NiCl_4$] and d) [BnzV][$ZnCl_4$]. Brown and blue spheres represent C and N atoms, respectively, while purple, blue, light grey and silver tetrahedra represent $[MnCl_4]^{2-}$, $[CoCl_4]^{2-}$, $[NiCl_4]^{2-}$, and $[ZnCl_4]^{2-}$, respectively. H atoms are omitted for clarity.

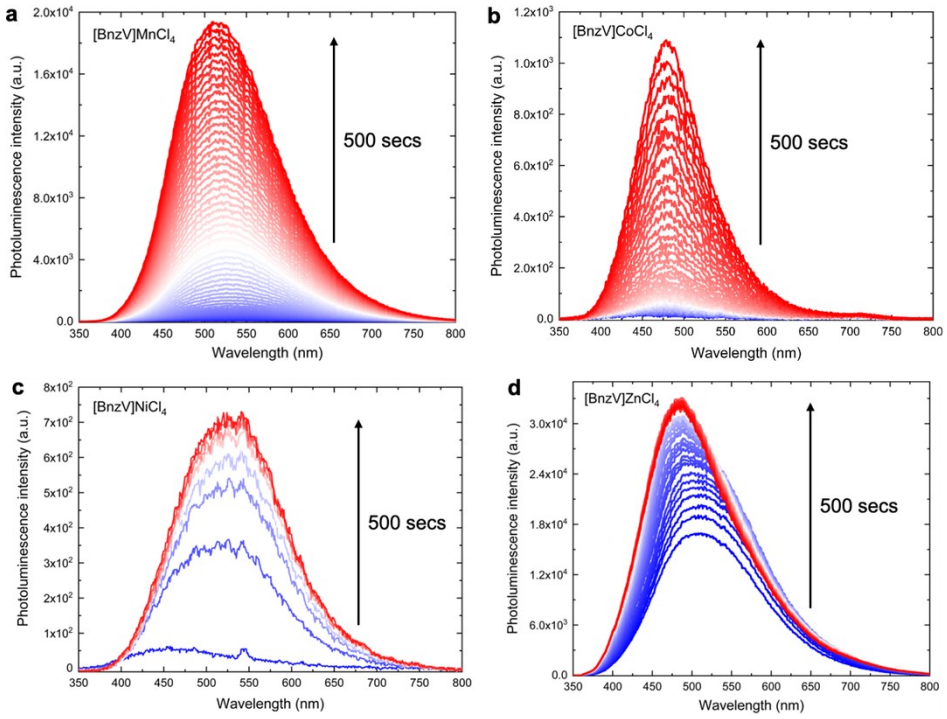

Figure S4. Photoluminescence evolution of a) [BnzV][$MnCl_4$], b) [BnzV][$CoCl_4$], c) [BnzV][$NiCl_4$] and d) [BnzV][$ZnCl_4$] during light soaking with 325 nm UV for 500 seconds.

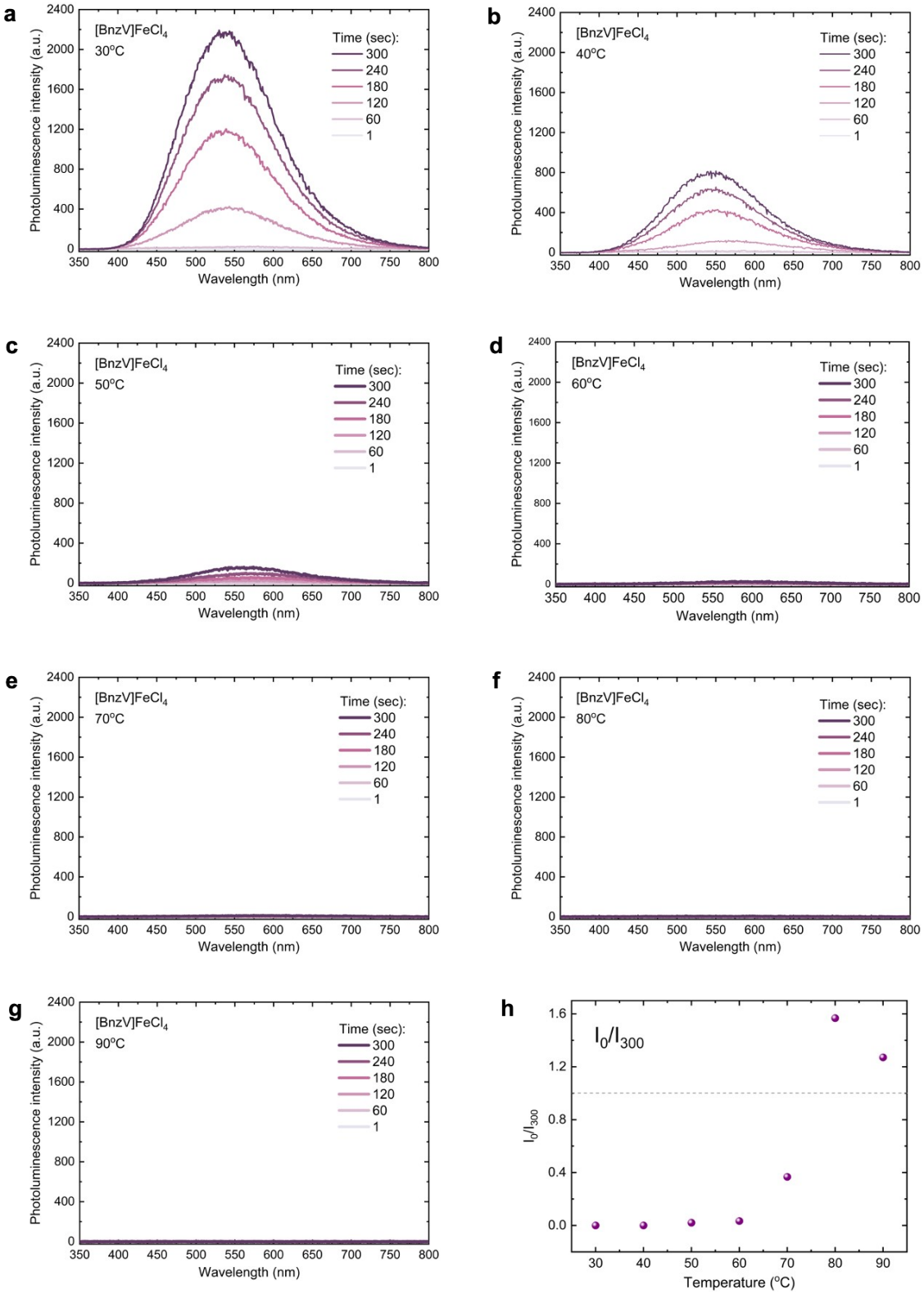

Figure S5. Temperature-dependent photoluminescence (PL) spectra evolution of [BnzV][$FeCl_4$] at a) 30°C, b) 40°C, c) 50°C, d) 60°C, e) 70°C, f) 80°C, and g) 90°C. j) Normalized PL intensity as a function of temperature at 1 second and 300 seconds of irradiation.

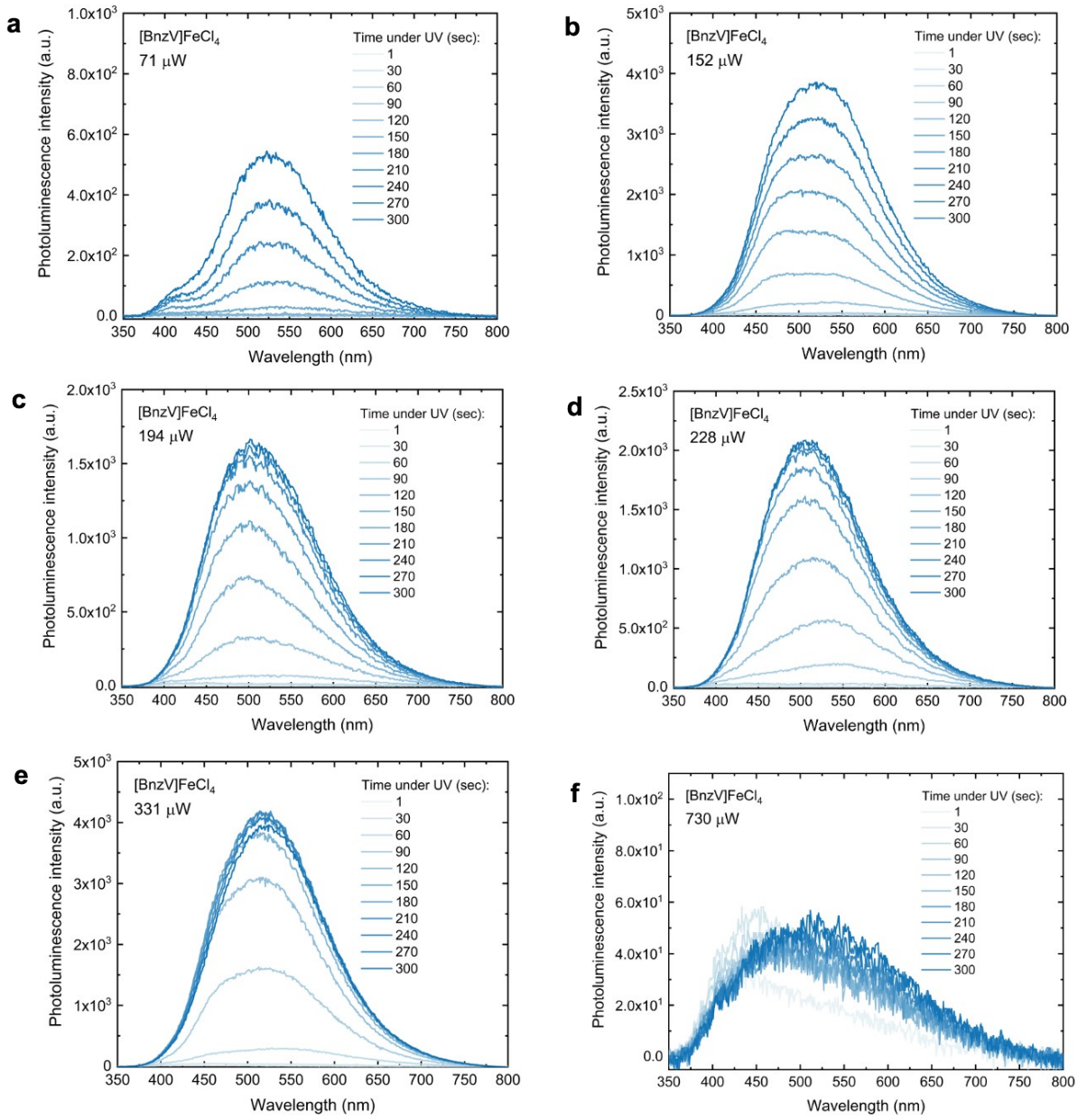

Figure S6. Power-dependent photoluminescence (PL) spectra of [BnzV][$FeCl_4$] over time at various excitation powers of 71, 152, 194, 228, 331, and 730 μWs.

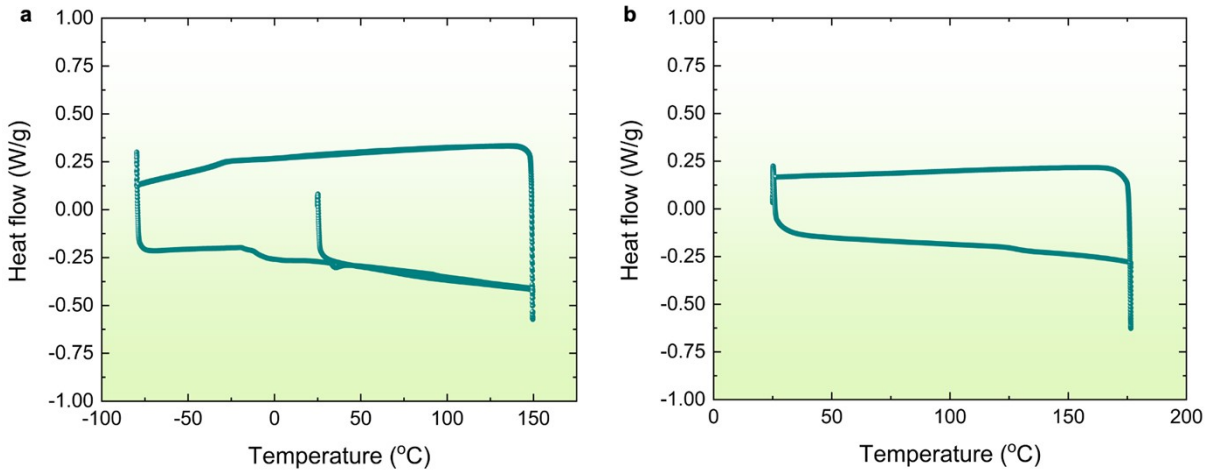

Figure S7. Differential scanning calorimetry (DSC) thermographs of [BnzV][$FeCl_4$] in the range of temperatures between a) -80 to 150°C and b) 25 to 180°C.

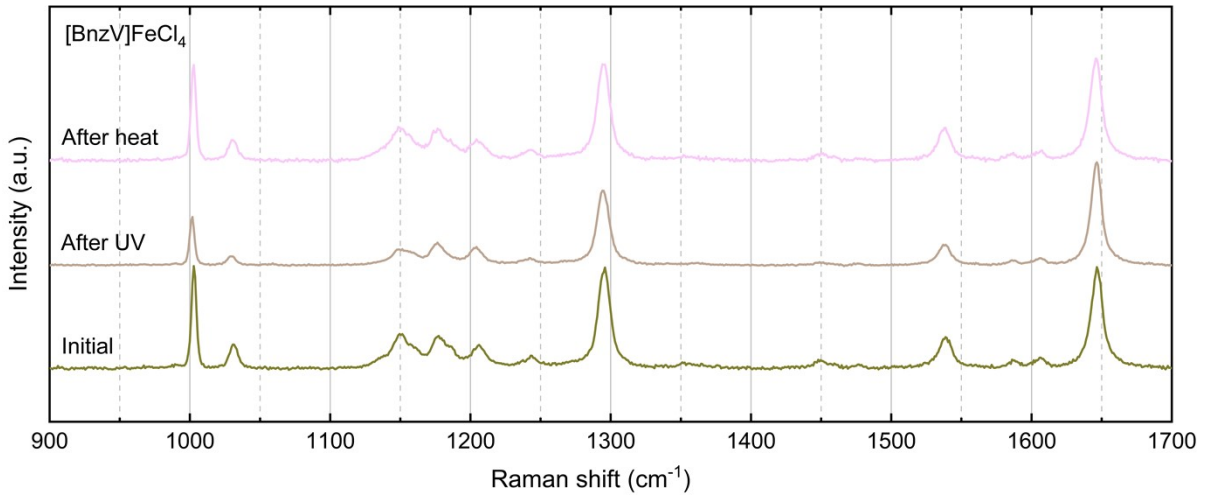

Figure S8. Raman spectra of as synthesized [BnzV][$FeCl_4$], after 6 hours of UV lamp illumination at 365 nm, and after 10 minutes of heating at 70°C (having undergone continuous UV illumination before). Detailed peak assignments are provided in **Table S3**.

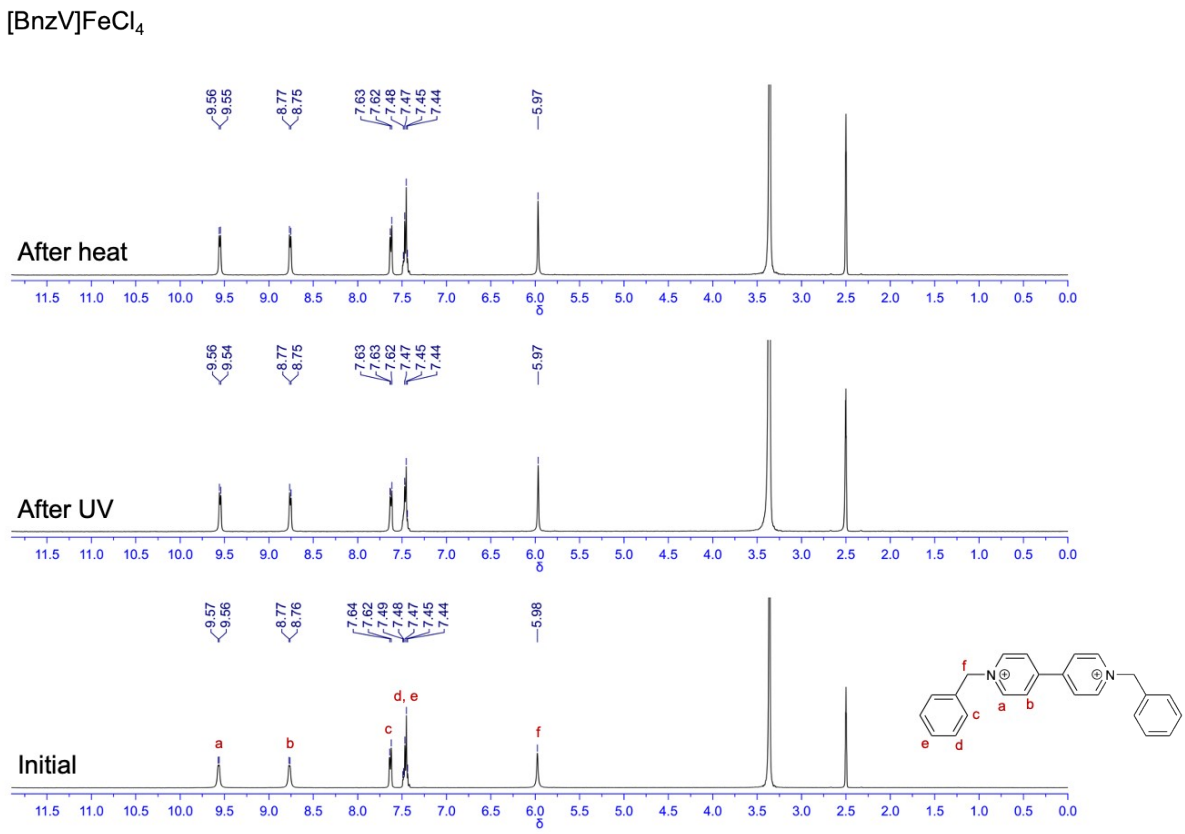

Figure S9. Nuclear magnetic resonance (NMR) spectra of as synthesized [BnzV][$FeCl_4$], after 6 hours of UV lamp illumination at 365 nm, and after 10 minutes of heating at 70°C (having undergone continuous UV illumination before). Inset shows the molecular structure of [BnzV] molecule with the corresponding peak assignment.

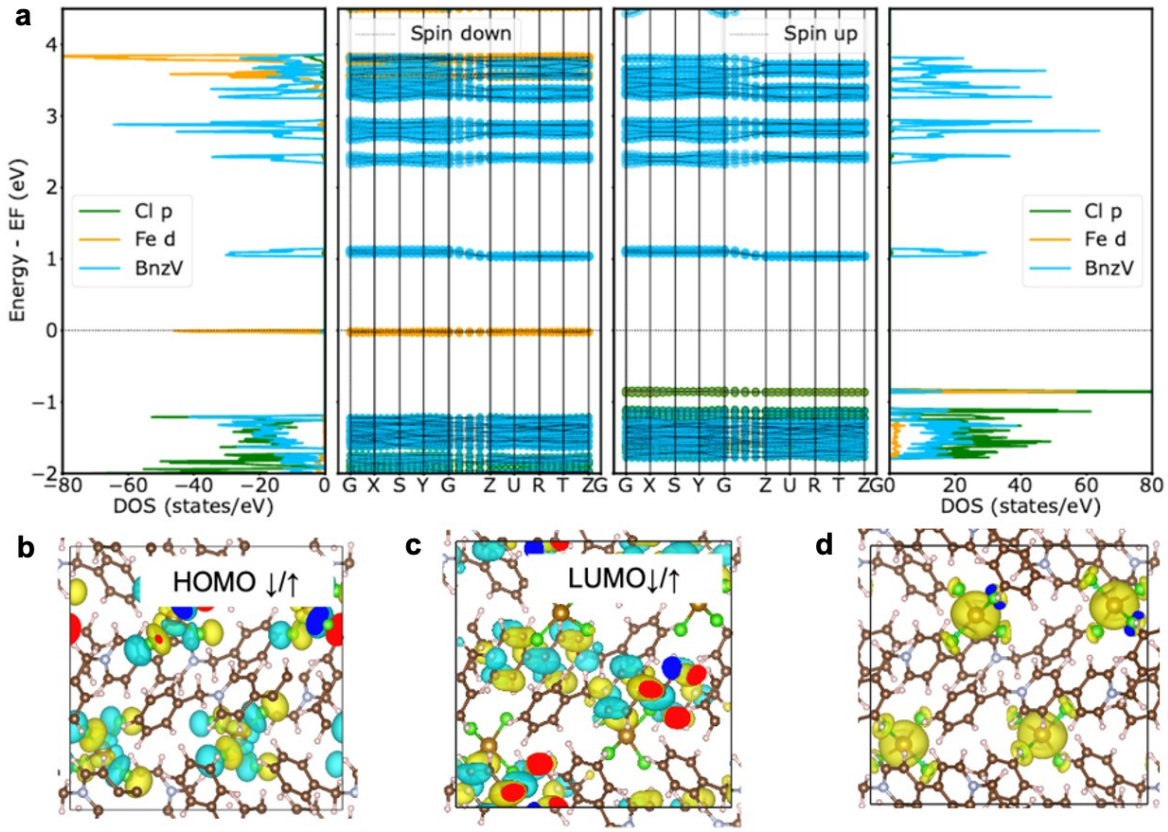

Figure S10. DFT Calculation Part I. Ground State.

a) The energy band structure along a high symmetry k-path and the corresponding partial density of states (PDOS) of the [BnzV][$FeCl_4$] compound in its ground state. The left and right sections illustrate the energy bands of spin-up and spin-down channels, respectively. The positions of the energy bands are depicted relative to the Fermi level. Horizontal dashed lines at 0 eV denote the Fermi level for spin-up and spin-down channels.

b) The isosurface of the HOMO and c) LUMO of the [BnzV][$FeCl_4$] compound in the ground state. The isovalue is 2×10^{-8}. The yellow and cyan colours denote (+) and (-) part of the wavefunctions respectively.

d) The isosurface of the spin density of the [BnzV][$FeCl_4$] compound in the ground state. The isovalue is 0.01.

Supplementary note on Figure S10:

Figure S10a presents the energy band structure along a high symmetry k-path and the corresponding partial density of states (PDOS) of the [BnzV][$FeCl_4$] compound in its ground state. The energy bands below the Fermi level are occupied, while those above the Fermi level are empty. According to this, no unoccupied Fe 3*d* bands exist in the spin-up channel. Conversely, only one occupied Fe 3*d* band is in the spin-down channel. This band is highly

localised right below the Fermi level, denoting itself as the highest occupied spin-down band of the whole [BnzV][$FeCl_4$]. The orbital at the Gamma point of this band, called the highest occupied molecular orbital of the spin-down channel HOMO↓, is shown in **Figure S10b**. Its spin-up counterpart is also highly localised, positioned 0.8 eV lower in energy, and resides within the highest occupied spin-up band. This orbital is so-called the HOMO↑. The unoccupied spin-down Fe 3*d* bands are localised around 4.1 eV above the Fermi level. The remaining occupied spin-up Fe 3*d* states are delocalised and dominate the energy range from -6.5 to -5.0 eV. This result indicates that there are one Fe 3*d* state completely filled and four Fe 3*d* states half-filled, indicative of a Fe^{2+} oxidation state with an electronic configuration of $3d^6$. The lowest unoccupied bands of spin-up and spin-down channels originate from the $[BnzV]^{2+}$ segment. They occur at the same energy, around 0.8 eV above the Fermi level, denoting no spin polarisation on the organic part of the compound. The corresponding lowest unoccupied molecular orbitals (LUMOs) is shown in **Figure S10c**. Consistently, the spin density is localised within the $[FeCl_4]^{2-}$ clusters, as depicted in **Figure S10d**.

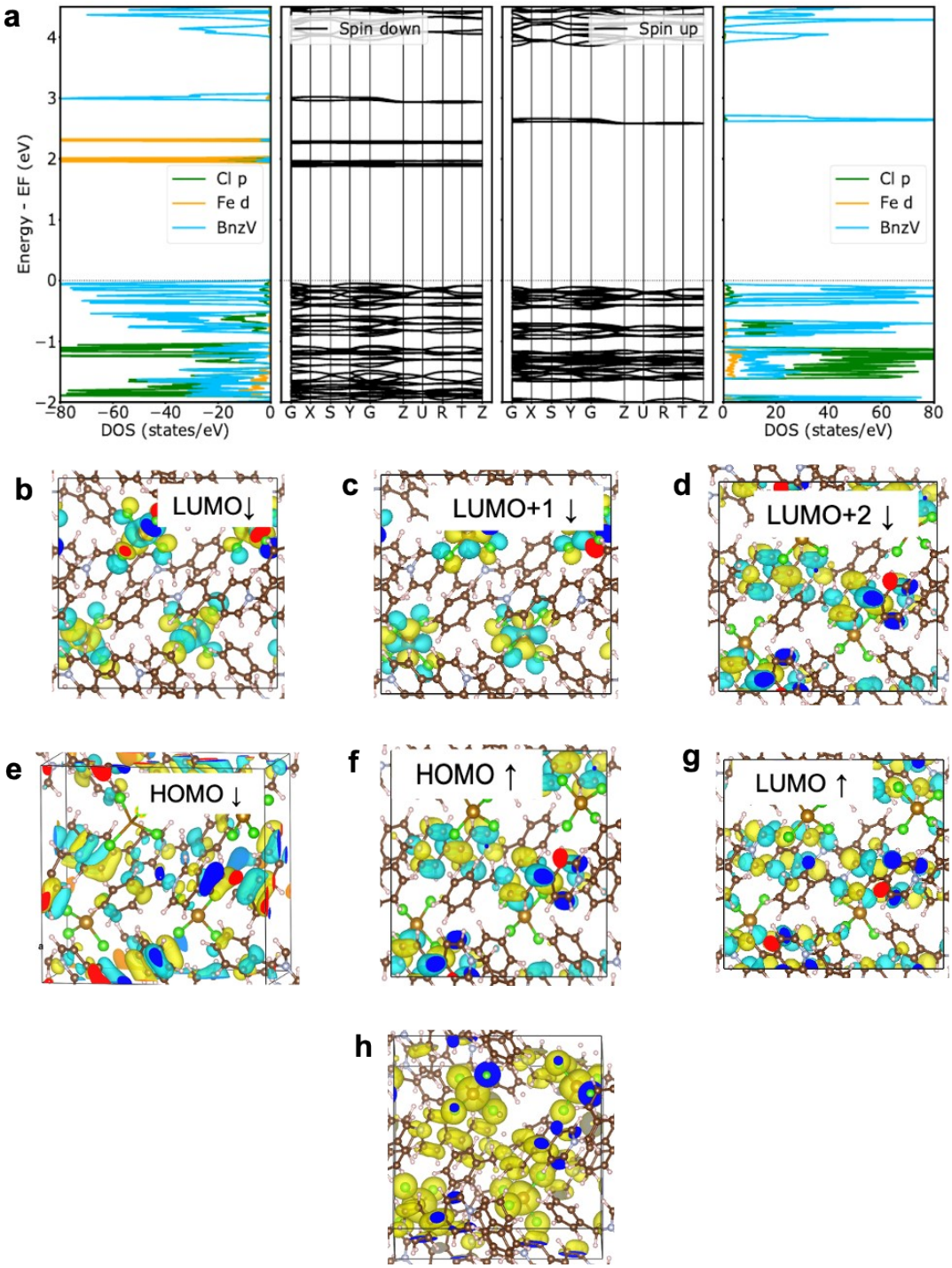

Figure S11 DFT Calculation Part II. After Photo-Induced Electron Transfer (PIET).

a) The energy band structure along a high symmetry k-path and the corresponding partial density of states (PDOS) of the [BnzV][$FeCl_4$] compound after PIET. The left and right sections illustrate the energy bands of spin-up and spin-down channels, respectively. The Fermi level of the spin-down channel is depicted as a dotted line at 0 eV, while the Fermi level of the spin-up channel is depicted as a dotted line at 2.7 eV. The positions of the energy bands are depicted relative to the spin-down Fermi level.

b) The isosurface of the LUMO$^{\downarrow}$, c) LUMO+1$^{\downarrow}$, d) LUMO+2$^{\downarrow}$, e) HOMO$^{\downarrow}$, f) HOMO$^{\uparrow}$ and g) LUMO$^{\uparrow}$ of the [BnzV][$FeCl_4$] compound after PIET. The isovalue is 2×10^{-8}. The yellow and cyan colours denote (+) and (-) part of the wavefunctions respectively.
h) The isosurface of the spin density of the BnzV$FeCl_4$ compound after PIET. The isovalue is 0.01.

Supplementary note on Figure S11:

In order to simulate the excited state of the [BnzV][$FeCl_4$] after the photoinduced electron transfer (PIET), the number of spin-up electrons per iron atom is constrained to be larger than that of spin-down electrons by six. This will constrain five electrons to occupy five Fe 3d orbitals, and the sixth electron must be spin up and, hence, is not allowed to complete any of the five Fe 3d orbitals. **Figure S11a** presents the energy band structure and the corresponding partial density of states (PDOS) obtained under this constraint. It should be noted that due to the constraint, the Fermi level of the spin-up channel is 2.7 eV higher than that of the spin-down channel. Accordingly, all spin-up Fe 3*d* bands are fulfilled and localised more than 8 eV below the spin-down Fermi level. However, all spin-down Fe 3*d* bands are unoccupied. Because of the reduction in number of electrons on the Fe 3*d* shells, these unoccupied lower down to 1.9 and 2.4 eV, lower than the $[BnzV]^{2+}$ LUMO$^{\downarrow}$, demonstrate themself as new LUMOs$^{\downarrow}$ (**Figure S11b,c**) of the whole compound. The $[BnzV]^{2+}$ LUMO$^{\downarrow}$ now becomes LUMO+2$^{\downarrow}$ (**Figure S11d**) of the whole compound. Its spin-up counterpart is still the LUMO$^{\uparrow}$ with slightly lower energy by about 0.3 eV. The new HOMO$^{\downarrow}$ also originates from the $[BnzV]^{2+}$, as shown in **Figure S11e**. The spin-up occupied Fe 3*d* bands are also lower down because of the reduction in the number of electrons on the Fe 3*d* shells. The new HOMO$^{\uparrow}$ is the old LUMO$^{\uparrow}$, which originates from the $[BnzV]^{2+}$ segment, and the new LUMO$^{\uparrow}$, also originates from the BnzV (**Figure S11f,g**). The spin distribution in **Figure S11h** consistently shows additional spin density on the $[BnzV]^{2+}$, denoting the sixth spin-up electron is transferred to the $[BnzV]^{2+}$.

Some comments on optical excitation:

- Before PIET, HOMO-LUMO transitions occur between $[FeCl_4]^{2-}$ to $[BnzV]^{2+}$.
- After PIET, HOMO$^{\downarrow}$-LUMO$^{\downarrow}$ transitions occur between the $[BnzV]^{2+}$ and $[FeCl_4]^{2-}$ but the HOMO$^{\uparrow}$-LUMO$^{\uparrow}$ is the intra $[BnzV]^{2+}$ molecular process (both HOMO$^{\uparrow}$ and LUMO$^{\uparrow}$) belong to $[BnzV]^{2+}$.

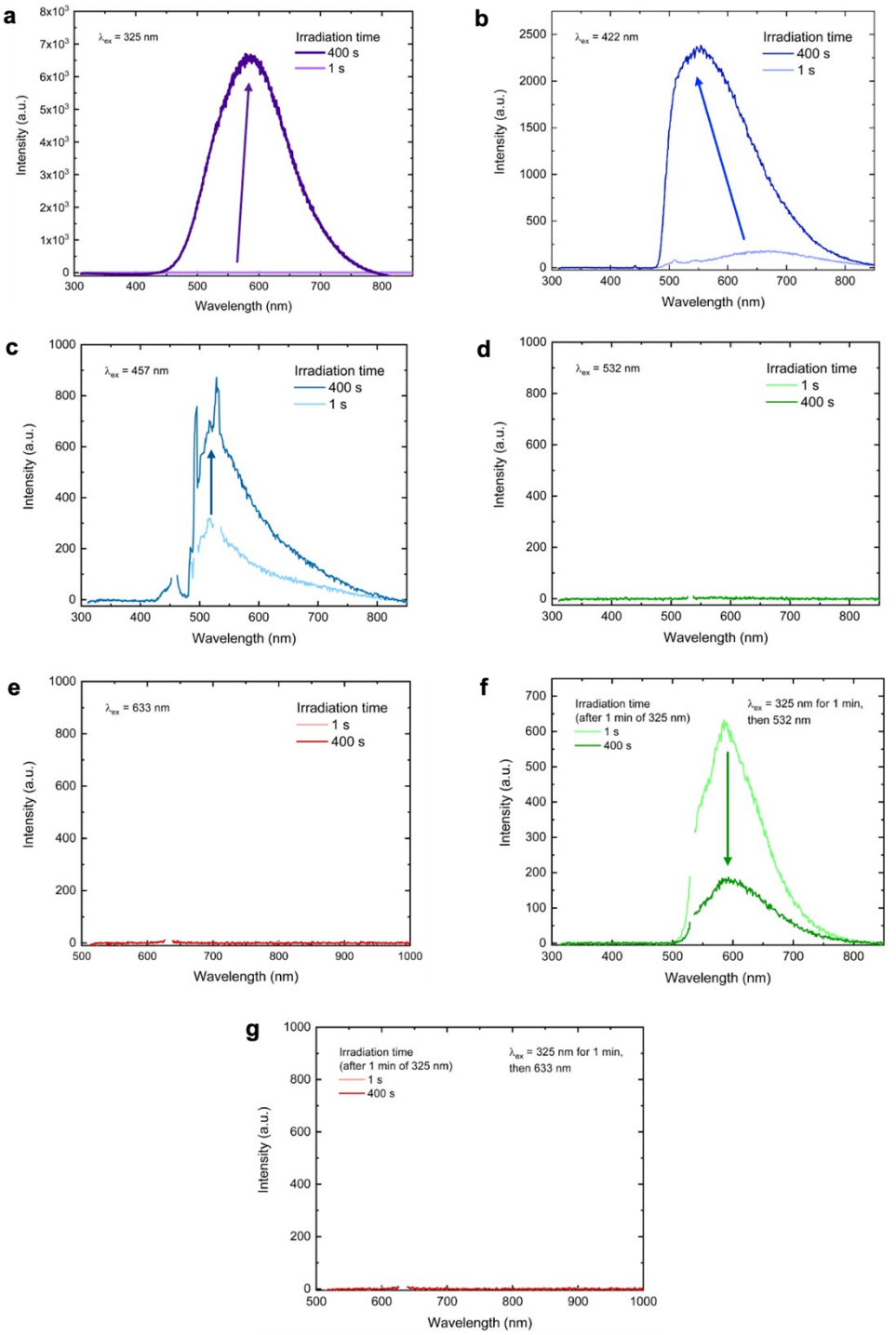

Figure 12. Photoluminescence (PL) spectra of [BnzV][$FeCl_4$] under continuous irradiation of a) 325 nm, b) 422 nm, c) 457 nm, d) 532 nm, and e633 nm excitation wavelengths. PL spectra of [BnzV][$FeCl_4$] with 325 nm "pre-excitation" followed by continuous irradiation with f) 532 nm and g) 633 nm light sources.

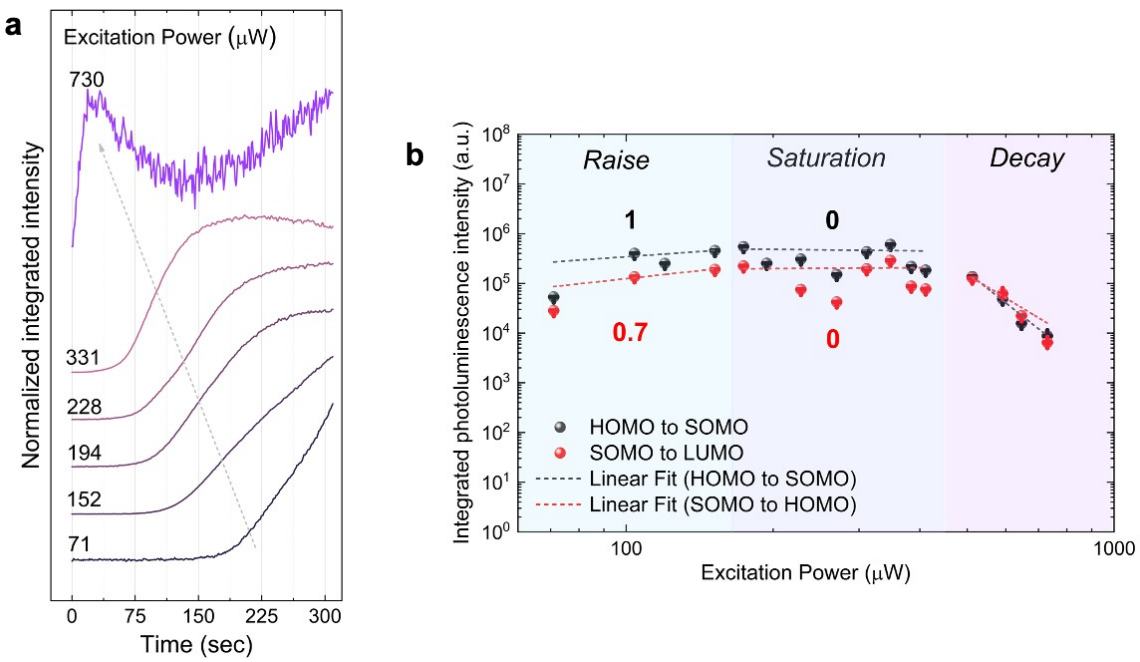

Figure 13. a) Normalized integrated photoluminescence (PL) intensity of [BnzV][FeCl4] over time at various excitation powers of 71, 152, 194, 228, 331, and 730 μWs. b) Excitation power-dependent integrated PL intensity, divided into raise, saturation, and decay regions, with linear fits for transitions such as HOMO (highest occupied molecular orbital) – SOMO (singly occupied molecular orbital) and SOMO – LUMO (lowest occupied molecular orbital) interactions.

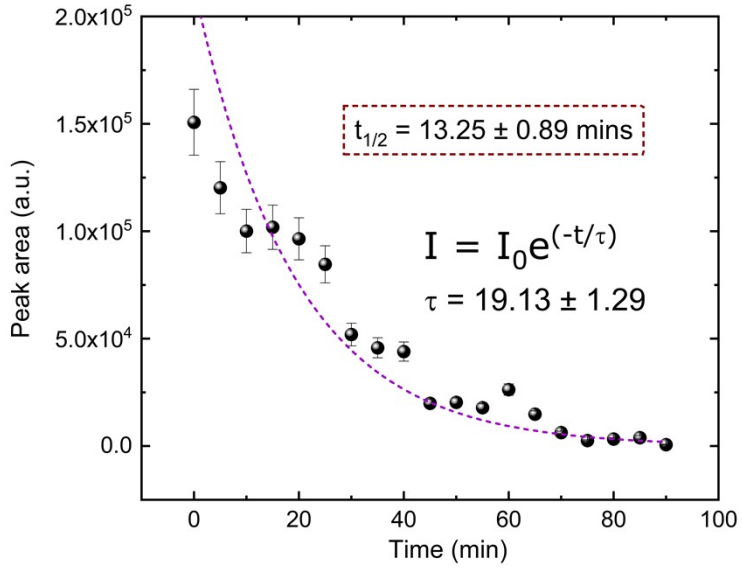

Figure S14. Exponential decay of peak area as the function of time fitted with a single exponential decay equation where I_0 is the initial intensity (or peak area) and τ is the decay time constant, which defines the rate of the exponential decrease. The calculated radical half-life is $t_{1/2}$ = 13.25 ± 0.89 mins.

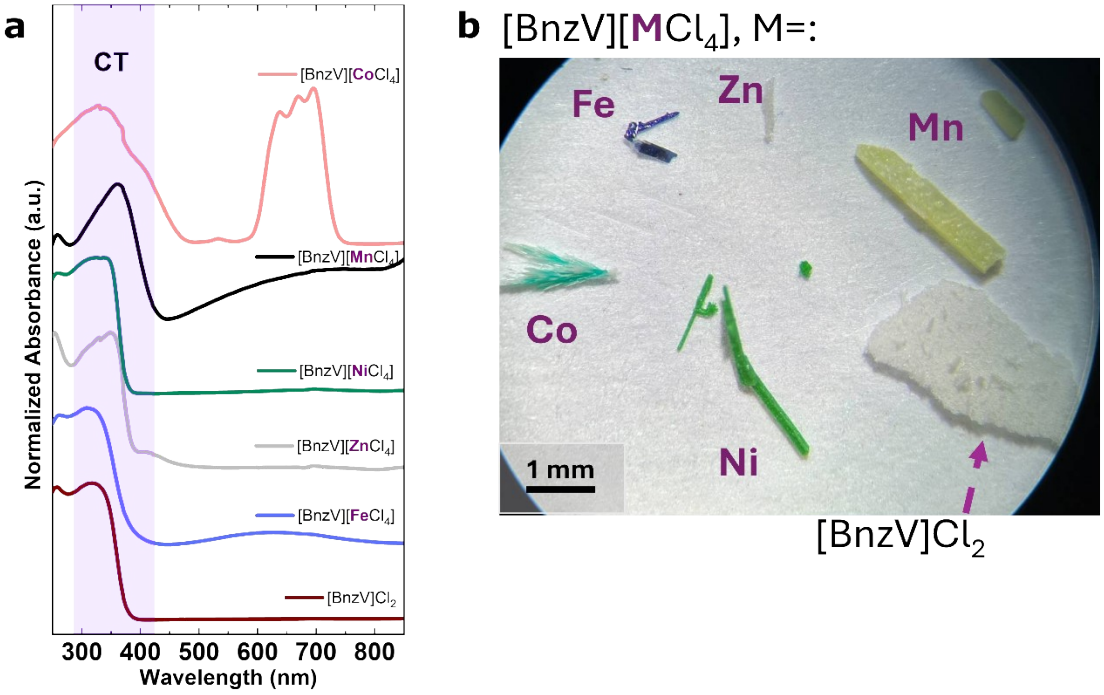

Figure S15. (a) UV–vis absorption spectra of single crystals of [BnzV][MCl_4] (M = Fe, Co, Ni, Zn, Mn) measured at room temperature; spectra are baseline-corrected, normalized, and vertically offset for clarity. The violet-shaded region highlights the charge-transfer absorption window typical for viologen hybrids. (b) Optical micrograph of representative single crystals with metal centers annotated (typical crystal colors: Fe—blue, Co—cyan/green, Ni—green, Zn—colorless, Mn—yellow). Scale bar: 1 mm.

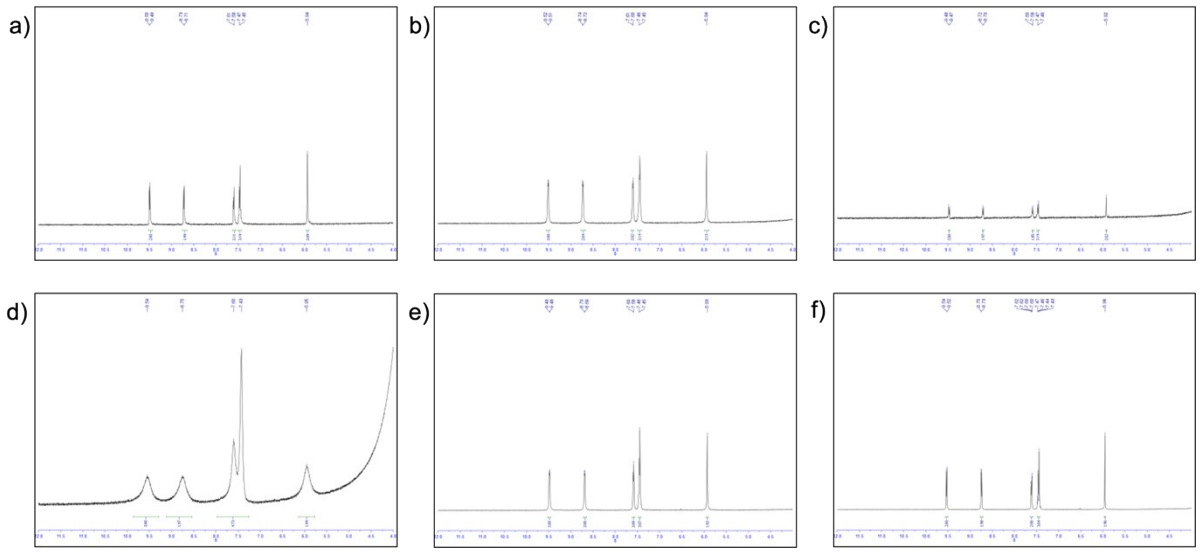

Figure S16. ^{1}H nuclear magnetic resonance spectra of a) [BnzV][Cl_2], b) [BnzV][$FeCl_4$], c) [BnzV][$ZnCl_4$], d) [BnzV][$MnCl_4$], e) [BnzV][$CoCl_4$], and f) [BnzV][$NiCl_4$], showing no change in the structures of the organic cations in each of the compound during single crystal synthesis. See **Figure S9** for the assignment of the peaks.

Table S1. Crystallographic and structure refinement data for [BnzV][$FeCl_4$], [BnzV][$MnCl_4$], and [BnzV][$CoCl_4$].[a]

	Compounds		
	[BnzV][$FeCl_4$]	[BnzV][$MnCl_4$]	[BnzV][$CoCl_4$]
Empirical formula	$C_{24}H_{22}Cl_4FeN_2$	$C_{24}H_{22}Cl_4MnN_2$	$C_{24}H_{22}Cl_4CoN_2$
Formula weight	536.08 g/mol	535.17 g/mol	539.16 g/mol
Temperature	100(2) K	100(2) K	100(2) K
Wavelength	0.71073 Å	0.71073 Å	0.71073 Å
Crystal size	0.120 x 0.200 x 0.240 mm	0.080 x 0.100 x 0.120 mm	0.040 x 0.080 x 0.220 mm^3
Crystal habit	blue block	pale yellow block	green needle
Crystal system	orthorhombic	orthorhombic	orthorhombic
Space group	P n a 21	P n a 21	P n a 21
Unit cell dimensions	a = 15.9309(13) Å	a = 16.0091(10) Å	a = 15.9764(13) Å
	α = 90°	α = 90°	α = 90°
	b = 15.5089(14) Å	b = 15.5747(9) Å	b = 15.4921(14) Å
	β = 90°	β = 90°	β = 90°
	c = 9.4926(7) Å	c = 9.4278(6) Å	c = 9.4426(7) Å
	γ = 90°	γ = 90°	γ = 90°
Volume	2345.3(3) $Å^3$	2350.7(2) $Å^3$	2337.1(3) $Å^3$
Z	4	4	4
Density	1.518 g/cm^3	1.512 g/cm^3	1.532 g/cm^3
Absorption coefficient	1.114 mm^{-1}	1.031 mm^{-1}	1.207 mm^{-1}
F(000)	1096	1092	1100
Theta range for data collection	2.52 to 34.98°	2.54 to 36.38°	2.53 to 31.51°
Reflections collected	64447	40331	45008
Coverage of independent reflections	99.9%	98.7%	99.8%
Absorption correction	Multi-Scan	Multi-Scan	Multi-Scan
Max. and min. transmission	0.8780 and 0.7760	0.9220 and 0.8860	0.9530 and 0.7770
Function minimized	$\Sigma w(F_o^2 - F_c^2)^2$	$\Sigma w(F_o^2 - F_c^2)^2$	$\Sigma w(F_o^2 - F_c^2)^2$
Data / restraints / parameters	9465 / 1 / 280	10157 / 1 / 281	7519 / 1 / 281
Goodness-of-fit on F^2	1.025	1.028	1.041
Δ/σmax	0.003	0.001	0.001
Final *R* indices	7064 data;	8031 data;	6385 data;
[I > 2σ(I)]	R1 = 0.0398,	R1 = 0.0444,	R1 = 0.0424,
	wR2 = 0.0650	wR2 = 0.0925	wR2 = 0.0912
R indices [all data]	R1 = 0.0744,	R1 = 0.0692,	R1 = 0.0594,
	wR2 = 0.0737	wR2 = 0.1041	wR2 = 0.1027
Largest diff. peak and hole	0.375 and -0.468 $eÅ^{-3}$	0.575 and -0.870 $eÅ^{-3}$	0.856 and -0.732 $eÅ^{-3}$
R.M.S. deviation from mean	0.087 $eÅ^{-3}$	0.105 $eÅ^{-3}$	0.094 $eÅ^{-3}$

[a] $R = \Sigma||F_o| - |F_c||/\Sigma|F_o|$, $wR = \{\Sigma[w(|F_o|^2 - |F_c|^2)^2]/\Sigma[w(|F_o|^4)]\}^{1/2}$ and [BnzV][$FeCl_4$], $w = 1/[\sigma^2(F_o^2) + (0.0231P)^2 + 0.3770P]$; [BnzV][$MnCl_4$], $w = 1/[\sigma^2(F_o^2) + (0.0397P)^2]$; [BnzV][$CoCl_4$], $w = 1/[\sigma^2(F_o^2) + (0.0412P)^2 + 0.9219P]$ where $P = (F_o^2+2F_c^2)/3$.

Table S2. Crystallographic and structure refinement data for [BnzV][$NiCl_4$] and [BnzV][$ZnCl_4$]. [a]

	Compounds	
	[BnzV][$NiCl_4$]	[BnzV][$ZnCl_4$]
Empirical formula	$C_{24}H_{22}Cl_4N_2Ni$	$C_{24}H_{22}Cl_4N_2Zn$
Formula weight	538.94 g/mol	545.60 g/mol
Temperature	100(2) K	100(2) K
Wavelength	0.71073 Å	0.71073 Å
Crystal size	0.010 x 0.020 x 0.220 mm^3	0.060 x 0.080 x 0.120 mm^3
Crystal habit	blue needle	colorless block
Crystal system	orthorhombic	orthorhombic
Space group	P n m a	P n a 21
Unit cell dimensions	a = 14.8985(11) Å	a = 15.9848(14) Å
	α = 90°	α = 90°
	b = 9.7134(9) Å	b = 15.5041(14) Å
	β = 90°	β = 90°
	c = 15.8906(12) Å	c = 9.4514(7) Å
	γ = 90°	γ = 90°
Volume	2299.6(3) $Å^3$	2342.3(3) $Å^3$
Z	4	4
Density	1.557 g/cm^3	1.547 g/cm^3
Absorption coefficient	1.324 mm^{-1}	1.520 mm^{-1}
F(000)	1104	1112
Theta range for data collection	2.46 to 29.59°	2.52 to 33.13°
Reflections collected	36003	49307
Coverage of independent reflections	99.9%	99.8%
Absorption correction	Multi-Scan	Multi-Scan
Max. and min. transmission	0.9870 and 0.7590	0.9140 and 0.8390
Function minimized	$\Sigma\, w(F_o^2 - F_c^2)^2$	$\Sigma\, w(F_o^2 - F_c^2)^2$
Data / restraints / parameters	3402 / 327 / 266	7337 / 1 / 281
Goodness-of-fit on F^2	1.016	1.077
Δ/σmax	0.003	0.001
Final *R* indices	2391 data;	6107 data;
[I > 2σ(I)]	R1 = 0.0694,	R1 = 0.0472,
	wR2 = 0.1776	wR2 = 0.1040
R indices [all data]	R1 = 0.1088,	R1 = 0.0691,
	wR2 = 0.2184	wR2 = 0.1239
Largest diff. peak and hole	1.955 and -1.693 $eÅ^{-3}$	1.115 and -1.204 $eÅ^{-3}$
R.M.S. deviation from mean	0.138 $eÅ^{-3}$	0.120 $eÅ^{-3}$

[a] $R = \Sigma||F_o| - |F_c||/\Sigma|F_o|$, $wR = \{\Sigma[w(|F_o|^2 - |F_c|^2)^2]/\Sigma[w(|F_o|^4)]\}^{1/2}$ and [BnzV][$NiCl_4$], $w = 1/[\sigma^2(F_o^2) + (0.0992P)^2 + 11.5518P]$; [BnzV][$ZnCl_4$], $w = 1/[\sigma^2(F_o^2) + (0.0507P)^2 + 2.4309P]$ where $P = (F_o^2 + 2F_c^2)/3$.

Table S3. Raman shifts values of experimental (as synthesized) [BnzV][$FeCl_4$] and calculated $[BnzV]^{2+}$ and $[BnzV]^{\bullet+}$ along with their corresponding vibrational modes assignments.

Experimental (as synthesized) [BnzV][$FeCl_4$] Raman shift (cm^{-1})	**Calculated $[BnzV]^{2+}$ Raman shift (cm^{-1})**	**Calculated $[BnzV]^{\bullet+}$ Raman shift (cm^{-1})**	**Assignments**
1003	1008	1006	Out-of-plane of ring
1030	1041	1027	C-N and C-C stretching (ring breathing vibration)
1150	1095	-	C-N intra-ring stretching
1175	-	1171	N-C-C scissors vibration (bonds between benzil and viologen rings)
1205	1224	1213	C-H inner-ring stretching
1243	1235	1259	H-C-C in-plane bending of the ring
1295	1298	-	C-C inter-ring vibration + H-C-C inter-ring bending
1353	-	1362	C-C inter-ring vibration
1447	1449	-	C-H asymmetric bending
1477	1476	-	C-H vibration
1538	1538	1537	H-C-C bending + C-N stretching
1647	1662	1676	C-C inner ring vibration

Table S4. Shortest distances between Cl atoms (in $[MCl_4]^{2-}$) and N atoms (in BnzV) (Å), where M is Fe, Zn, Co, or Mn.

***d*-element**	**Distance (Å)**
Fe	3.441
Zn	3.741
Co	3.735
Mn	3.488

Table S5. Electron transfer paths and the corresponding donor-acceptor distances in the reported viologen-based compounds.

Viologen-based compounds	Electron transfer paths	Electron transfer distances (Å)	Refs.
$(C_{13}H_{16}N_2O_2)_2InCl_6 \cdot Cl$	Cl···N, Cl···Pyridine ring	3.23~3.49	8
$\{[Zn_2(cbbpy)_2(IPA)_2] \cdot 4H_2O\}n$	O···N	3.33~4.23	9
$\{[Zn(cbbpy)(PTA)_{0.5}Cl] \cdot 2H_2O\}n$	Cl···H-C, O···H-C-N	3.14~3.54	10
$[Zn_7(bpybc)_3(o\text{-}BDC)_6] \cdot 2NO_3 \cdot 6H_2O$	O···N	3.27~3.72	11
$[PV]Zn_3(m\text{-}BDC)_4] \cdot H_2O$	O···N	3.37~3.49	12

References

1. Momma, K.; Izumi, F. An Integrated Three-Dimensional Visualization System VESTA Using wxWidgets. *Commission on Crystallogr. Comput.* **2006**, *7*, 106–119.
2. Blöchl, P. E. Projector Augmented-Wave Method. *Phys. Rev. B* **1994**, *50* (24), 17953. https://doi.org/10.1103/PhysRevB.50.17953.
3. Kresse, G.; Joubert, D. From Ultrasoft Pseudopotentials to the Projector Augmented-Wave Method. *Phys. Rev. B* **1999**, *59* (3), 1758. https://doi.org/10.1103/PhysRevB.59.1758.
4. Kresse, G.; Furthmüller, J. Efficient Iterative Schemes for Ab Initio Total-Energy Calculations Using a Plane-Wave Basis Set. *Phys. Rev. B. Condens. Matter* **1996**, *54* (16), 11169–11186. https://doi.org/10.1103/PHYSREVB.54.11169.
5. Perdew, J. P.; Burke, K.; Ernzerhof, M. Generalized Gradient Approximation Made Simple. *Phys. Rev. Lett.* **1996**, *77* (18), 3865. https://doi.org/10.1103/PhysRevLett.77.3865.
6. Dudarev, S. L.; Botton, G. A.; Savrasov, S. Y.; Humphreys, C. J.; Sutton, A. P. Electron-Energy-Loss Spectra and the Structural Stability of Nickel Oxide: An LSDA+U Study. *Phys. Rev. B* **1998**, *57* (3), 1505. https://doi.org/10.1103/PhysRevB.57.1505.
7. Grimme, S.; Antony, J.; Ehrlich, S.; Krieg, H. A Consistent and Accurate Ab Initio Parametrization of Density Functional Dispersion Correction (DFT-D) for the 94 Elements H-Pu. *J. Chem. Phys.* **2010**, *132* (15). https://doi.org/10.1063/1.3382344/926936.
8. Pan, Q. Y.; Sun, M. E.; Zhang, C.; Li, L. K.; Liu, H. L.; Li, K. J.; Li, H. Y.; Zang, S. Q. A Multi-Responsive Indium-Viologen Hybrid with Ultrafast-Response Photochromism and Electrochromism. *Chem. Commun.* **2021**, *57* (86), 11394–11397. https://doi.org/10.1039/D1CC05070B.
9. Yang, D. D. *et al.* Multistimuli-Responsive Materials Based on Zn(II)-Viologen Coordination Polymers and Their Applications in Inkless Print and Anticounterfeiting. *Inorg. Chem.* **61**, 7513-7522, doi:10.1021/acs.inorgchem.2c00599 (2022).
10. Yang, D.-D. *et al.* UV and X-ray Dual Photochromism of Two Zn(II)-Viologen Coordination Polymers and Fast Decoloration by Hydrogen Chloride. *Cryst. Growth Des.* **22**, 6224-6231, doi:10.1021/acs.cgd.2c00778 (2022).
11. Li, S. L. *et al.* X-ray and UV Dual Photochromism, Thermochromism, Electrochromism, and Amine-Selective Chemochromism in an Anderson-like Zn(7)

Cluster-Based 7-Fold Interpenetrated Framework. *J. Am. Chem. Soc.* **141**, 12663-12672, doi:10.1021/jacs.9b04930 (2019).

12. Hu, S., You, M., Chen, S. & Fu, Z. A fast-response photochromic host–guest coordination polymer with a close-packed stacking structure. *CrystEngComm* **18**, 7221-7224, doi:10.1039/c6ce00727a (2016).